FISEVIER

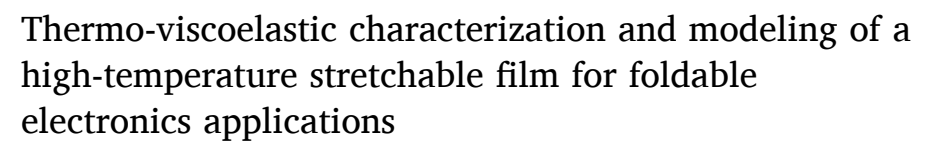
Contents lists available at ScienceDirect

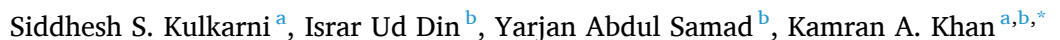
International Journal of Engineering Science

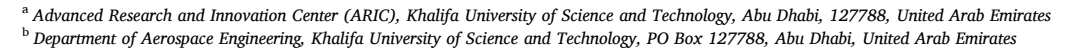
journal homepage: www.elsevier.com/locate/ijengsci



Full Length Article







ARTICLE INFO

Keywords: Stretchable electronics Foldable electronics Film Characterization Thermo-viscoelastic modeling Long-term stress based integral viscoelastic

ABSTRACT

Foldable electronics with high thermal stability, flexibility and stretchability enable emerging applications such as soft robotics, electronic skins, human-machine interfaces, and foldable displays. This study presents a detailed thermo-mechanical characterization and modeling of BeyolexTM, a recently developed non-silicone-based thermoset polymeric substrate used in stretchable electronics. During operation, BeyolexTM undergoes diverse loading histories, motivating a comprehensive experimental program. We performed tensile tests at various loading rates, along with stress relaxation, creep, and cyclic loading tests. To replicate in-service thermal conditions, experiments were conducted at 25 °C, 75 °C, 90 °C, 125 °C, and 150 °C, covering the full operational temperature range of the material. A finite viscoelasticity-based integral model was developed, formulated from the material's equilibrium (long-term stress) response. The model was further enhanced to capture thermal effects and stress softening behavior. An iterative root-finding algorithm was developed to simulate the model's response to both displacementcontrolled and force-controlled loading conditions. Finally, a calibration methodology was implemented to fit the model parameters and assess its performance. Simulated results under various loading histories showed reasonable agreement with experimental data, supporting the model's capability to represent BeyolexTM's thermo-mechanical behavior.

1. Introduction

Polymeric materials with outstanding properties such as thermal stability, good transparency, and high elasticity are promising candidates for developing stretchable electronic devices and foldable gadgets. These highly stretchable materials can serve as substrates in the fabrication of such devices using modern additive manufacturing techniques like direct ink writing (DIW) (Yang et al., 2021). Unlike rigid circuit board technologies, stretchable electronic devices offer large stretchability and foldability without compromising functionality, enabling a wide range of advanced applications. These include human–machine interfaces, soft robotics, stretchable energy harvesters, and flexible sensing patches (Amjadi et al., 2015; Malik et al., 2023; Trung & Lee, 2017; Wang et al., 2022). Such materials also have the potential for direct integration with soft materials and curvilinear surfaces, such as biological tissues, to function as sensing patches (Fan et al., 2014). For an on-skin electronic device to operate successfully, it must exhibit a

E-mail address: kamran.khan@ku.ac.ae (K.A. Khan).

https://doi.org/10.1016/j.ijengsci.2025.104352

Received 3 May 2025; Received in revised form 5 July 2025; Accepted 8 July 2025 Available online 19 July 2025

0020-7225/© 2025 The Authors. Published by Elsevier Ltd. This is an open access article under the CC BY-NC-ND license (http://creativecommons.org/licenses/by-nc-nd/4.0/).

^{*} Corresponding author.

mechanical response similar to human skin when subjected to various modes of large deformation (Malik et al., 2023). Therefore, detailed characterization and modeling of the thermo-mechanical behavior of these novel, highly stretchable substrate films are essential for the development of more efficient and conformal electronic devices.

Substrate films used in wearable electronic devices must withstand significant stretching and varying deformation rates during use. For example, a sports gadget should perform reliably under high strain levels and corresponding strain rates. Human skin can typically stretch up to 30 % strain Malik et al. (2023), and wearable devices must tolerate similar deformation without damage. The wearable gadget should also withstand such high strain values without any damage. Various soft polymers are employed as substrates in stretchable electronics due to their high stretchability, along with adequate performance under elevated temperatures and strain rates. Wang et al. (2022) developed a 16-channel sensing patch using a styrene-ethylene-butylene-styrene (SEBS) thermoplastic elastomer (TPE), which demonstrated ultrahigh stretchability up to 400 % tensile strain and excellent durability under repetitive deformation.

Thermoplastic polyurethane (TPU) has been widely used in stretchable electronic systems due to its high stretchability requirements in such applications (Lee et al., 2022; Wu, 2019). However, Malik et al. (2023) employed a recently developed thermoset-based stretchable substrate, commercially known as BeyolexTM, in stretchable electronic systems. The BeyolexTM-based system was subjected to 200 cycles with a 30 % tensile strain. A linear elastic finite element model of the 100 µm thick BeyolexTM film was also presented (Malik et al., 2023). However, a detailed thermo-mechanical characterization of the BeyolexTM film is necessary to fully define its highly non-linear constitutive behavior, along with its temperature-dependent viscoelastic properties such as creep and stress relaxation. Such characterization will enable the design of more efficient and robust stretchable electronic systems using BeyolexTM film.

The hyperelasticity exhibited by Beyolex™ film can be modeled using two primary approaches: phenomenological and micromechanical models (Melly et al., 2021). Well-known examples of phenomenological models include the Neo-Hookean (Rivlin, 1948), Yeoh (Yeoh, 1990), Mooney-Rivlin (Mooney, 1940; Rivlin, 1948) (Invariant based) and Ogden (Ogden, 1972), Valanis-Landel (Valanis & Landel, 1967) (stretch-based) models, which use macroscopic continuum mechanics descriptions. In contrast, micromechanical models, such as the three-chain (Melly et al., 2021; Wang & Guth, 1952) and eight chain (Arruda & Boyce, 1993) models, are based on statistical mechanics theory to describe the free energy due to deformation, considering the orientation of long polymeric chains in the unit cell. However, these models, in their original hyperelastic formulation, are rate-independent and do not capture viscoelastic phenomena, such as stress relaxation and creep.

One of the earliest approaches to model rate-dependent finite strain responses in materials was developed by Pipkin and Rogers (1968) using a hereditary integral. Fung (1993) further simplified this model by assuming a multiplicative split of the instantaneous response functional into deformation and time-dependent terms, a concept that became known as quasi-linear viscoelasticity. Similarly, Holzapfel and Simo (1996) proposed an integral finite strain viscoelastic model based on a deviatoric-volumetric split of the deformation gradient tensor. The literature contains many other large strain integral viscoelastic models (Ahmed et al., 2024; Bernstein et al., 1963; Hoo Fatt & Ouyang, 2007; Pei et al., 2024; Wineman, 2009; Yang et al., 2000). Complementary to these integral approaches, thermodynamically motivated models based on internal variables also gained prominence. Eckart's theory (Eckart, 1940) introduced the concept of dissipation governed by hidden or internal variables. Rajagopal and Wineman (1992) further developed this idea by explicitly formulating evolution equation for internal variables to capture deformation-induced microstructural changes within a thermodynamically consistent framework. Bergstrom (1998) proposed a differential-type constitutive model for polymers, wherein an evolution law was defined based on micro-mechanism-inspired stress flow. Koprowski-Theiss et al. (2011) introduced an evolution law based on finite viscoelasticity, which has been adopted by many researchers (Hossain et al., 2020; Kulkarni et al., 2025; Liao et al., 2020). Although many differential-type constitutive laws exist in the literature, each Maxwell element introduces an additional internal variable, thereby increasing the dimensionality of the system of differential equations (Kulkarni et al., 2022). As more Maxwell elements are added, the computational cost and numerical complexity grow, which typically limits the number of elements used to maintain efficiency. In contrast, finite viscoelasticity-based integral models usually rely on hereditary integrals with kernels often represented by a Prony series, which can be computed efficiently. Unlike differential models, increasing the number of Prony terms does not significantly raise computational complexity, since internal state variables are not tracked. However, conventional integral models generally embed viscous effects within the instantaneous stress response, making it difficult to independently calibrate the elastic and viscous contributions. To overcome this limitation, we propose a novel finite viscoelasticity-based integral model that is formulated with respect to the long-term stress response. In this approach, the long-term stress explicitly represents the elastic component, allowing for separate and more straightforward calibration from the viscous response. This separation also facilitates the independent evaluation of thermal effects on the elastic (long-term) and viscous components, thereby enhancing the model's interpretability and applicability.

In this study, we present a detailed characterization of a recently developed non-silicone-based thermoset polymer film known as BeyolexTM. In the first phase of the characterization, thermal tests were conducted to investigate the film's thermal properties and phase transitions under thermal ramps. In the second phase, thermomechanical experimental program was devised for isothermal tensile loading which consisted of viscoelastic tests like single-step relaxation and creep tests across different temperatures. In the last phase, a finite viscoelasticity-based integral model was developed, formulated based on the material's equilibrium (long-term stress) response. The model was further enhanced to capture thermal effects and stress softening behavior. An iterative root-finding algorithm was developed to simulate the model's response to both displacement-controlled and force-controlled loading conditions. The experimental data were used to calibrate and model this highly stretchable film, supporting its application in the design and development of foldable electronic devices.

2. Materials and experiments

2.1. Materials

In this study, BeyolexTM, a non-silicone, thermoset polymer-based, highly stretchable, transparent film with a thickness of $100 \mu m$, was supplied by Panasonic, Japan. This novel material exhibits good elongation—up to 200 %—and high thermal resistance, with a decomposition temperature of approximately $300 \degree C$ (Malik et al., 2023). It was recently developed for the design and manufacture of flexible, stretchable, and pliable printed electronic systems intended for use in aerospace, automotive, healthcare, sensors, and robotics applications. The film is compatible with a wide range of functional inks, making it suitable as a substrate for the development of foldable electronic devices using the direct ink writing (DIW) technique.

2.2. Testing procedure

2.2.1. Thermal characterization

To investigate the thermal behavior of the BeyolexTM film, two thermal characterization techniques, i.e., differential scanning calorimetry (DSC) and thermogravimetric analysis (TGA) were employed. For the DSC test, samples weighing between 16 and 18 mg were placed in aluminum pans with lids supplied by Red Thermo Company. The tests were conducted using a TA Instruments DSC25 system with a heating rate of $^{\circ}$ C/min over a temperature range of $^{-30}$ $^{\circ}$ C to 250 $^{\circ}$ C. Results from three heating cycles were recorded. For thermogravimetric analysis, a TA Instruments SDT Q600 system was used to measure percentage mass loss and thermal degradation. Samples weighing between 13 and 15 mg were subjected to a temperature ramp from room temperature to 500 $^{\circ}$ C at a rate of 5 $^{\circ}$ C/min.

2.2.2. Thermo-mechanical experiments

The viscoelastic characteristics of the Beyolex™ film were investigated through thermo-mechanical testing using a dynamic mechanical analyzer (DMA). For this purpose, a TA Instruments Model Q800 was used to test rectangular Beyolex™ film samples under tensile loading conditions, as shown in Fig. 1. The thermo-mechanical characterization included isothermal monotonic and cyclic tensile tests conducted at three strain rates: 0.01, 0.001, and 0.0001 s⁻¹. Cyclic tests were further supplemented by step-cyclic experiments. Additionally, creep/creep recovery, single-step, and multi-step stress relaxation tests were performed using the same DMA setup. The isothermal test temperatures—25 °C, 75 °C, 90 °C, 125 °C, and 150 °C—were selected to reflect typical operating conditions that electronic systems may encounter during service. A preload of 0.001 N was applied prior to the start of each test. Each test was repeated at least three times, and the average representative response curve is presented in this study.

3. Results and discussion

3.1. Thermal tests

The thermal characterization results from differential scanning calorimetry (DSC) and thermogravimetric analysis (TGA) are presented in Fig. 2. The thermal characterization results from differential scanning calorimetry (DSC) and thermogravimetric analysis (TGA) are presented in Fig. 2(a). The first heating cycle was excluded from glass transition temperature (Tg) analysis. Based on the second and third heating cycles, the Tg of BeyolexTM samples was identified in the range of approximately 8 $^{\circ}$ C to 10 $^{\circ}$ C. No thermal

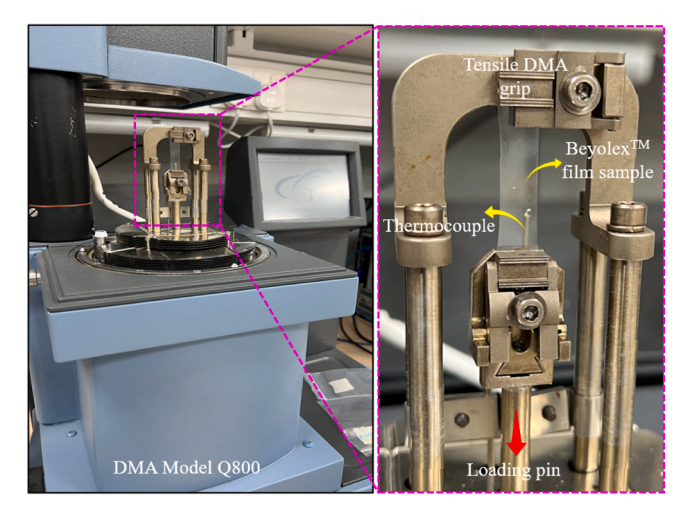


Fig. 1. Thermo-mechanical experimental test set-up in the dynamic mechanical analyzer (DMA).

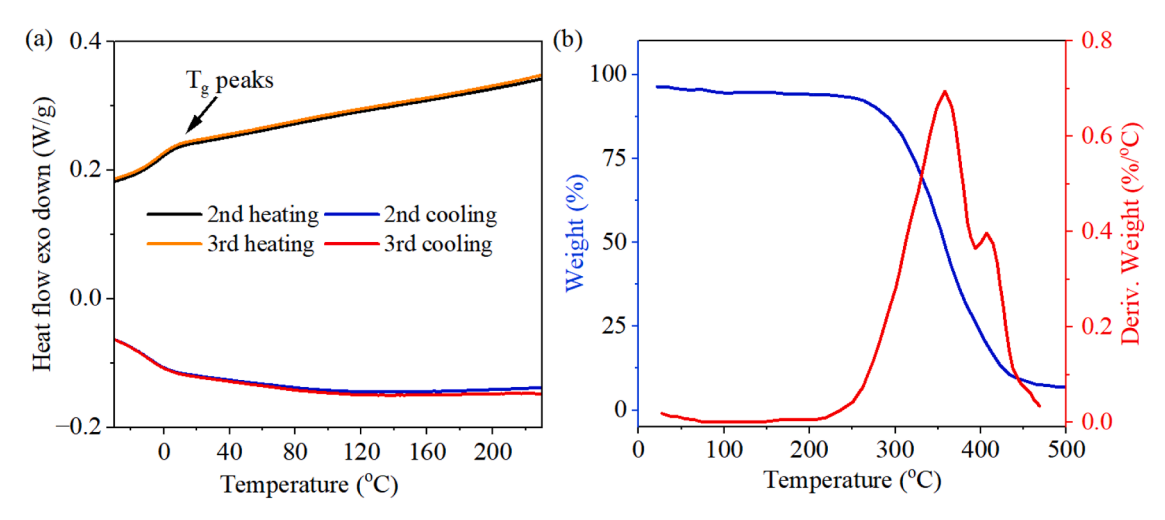


Fig. 2. Thermal characterization tests, (a) heating and cooling cycles in differential scanning calorimetry (DSC), (b) thermogravimetric analysis (TGA).

events were observed beyond the Tg up to 230 $^{\circ}$ C during the DSC tests. TGA tests were conducted from room temperature to 500 $^{\circ}$ C using the same heating rate as the DSC tests. The percentage of weight loss and its derivative with respect to temperature are plotted in Fig. 2(b). Minimal weight loss was observed up to approximately 270 $^{\circ}$ C, after which a rapid decrease in mass occurred. Around 15 % weight loss was recorded at 300 $^{\circ}$ C, increasing to approximately 93 % at 500 $^{\circ}$ C.

3.2. Thermo-mechanical tests

3.2.1. Isothermal monotonic tensile tests

Isothermal monotonic tensile tests were conducted at five temperatures: 25 °C, 75 °C, 90 °C, 125 °C, and 150 °C, as shown in Fig. 3. Three strain rates—0.0001 s⁻¹ (slow), 0.001 s⁻¹ (medium), and 0.01 s⁻¹ (high)—were selected to evaluate the rate-dependent behavior of the BeyolexTM film. Fig. 3 (a-c) illustrates the effect of temperature on the stress–strain response of the thermoset BeyolexTM film. The material exhibited non-linear mechanical behavior with only mild sensitivity to temperature across the tested range. According to prior studies, BeyolexTM can stretch up to 200 % strain with a maximum tensile strength of 16 MPa (Malik et al., 2023). However, for these tests, load and strain levels were limited by the 20 N capacity of the DMA force sensor. Therefore, all samples were stretched up to 120 % nominal tensile strain without fracture. Strain rate sensitivity at 25 °C and 150 °C is compared in Fig. 3(d), showing slightly more pronounced rate-dependence at room temperature. Overall, the BeyolexTM film demonstrated mild thermal and strain rate dependency under the given test parameters—an advantageous property for the development of foldable electronic systems.

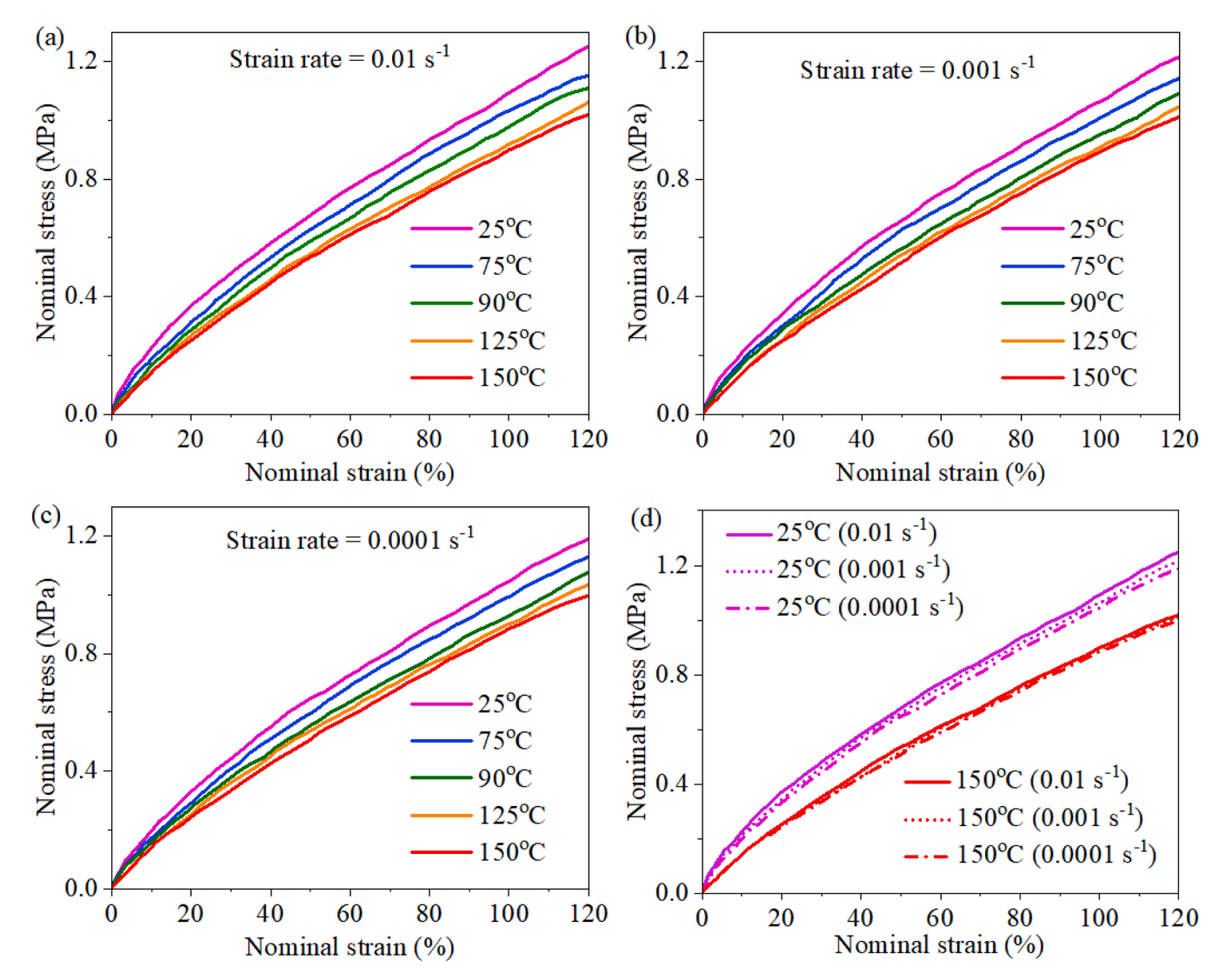
3.2.2. Loading-unloading cyclic tests

Cyclic tests were conducted at the same three strain rates $(0.01, 0.001, \text{ and } 0.0001 \text{ s}^{-1})$ as those used in the monotonic tensile tests, at test temperatures of 25 °C, 75 °C, 125 °C, and 150 °C. Fig. 4 presents the loading–unloading results, where samples were stretched up to a tensile strain of 70 %. It can be observed that, at higher strain rates, the stress levels are greater than those at lower strain rates for all isothermal conditions. Similar to the monotonic tests, strain rate dependency was more pronounced at room temperature, as shown in Fig. 4(a), compared to the higher temperature results.

Furthermore, Fig. 4 shows that the hysteresis loops at room temperature (Fig. 4a) are larger than those at elevated temperatures, indicating higher energy dissipation. Fig. 5 compares the step loading–unloading behavior of BeyolexTM film at a strain rate of 0.001 s⁻¹. A maximum tensile strain of 52 % was applied in three increments, without any pause between the loading and unloading cycles. The room temperature test in Fig. 5(a) again shows greater energy dissipation compared to higher temperature tests, consistent with the single-cycle results. Additionally, the step cyclic tests revealed a progressive reduction in stiffness with each cycle, indicating softening due to damage accumulation in the material. However, as noted by Bucchi et al. (2023), damage in polymer science is primarily associated with chain or link breakage, leading to a transition from a hard to a soft phase in the material. In contrast, the form of damage discussed in this work refers to network alterations or reorganizations that lead to stress softening during cyclic loading. Unlike chain breakage, this mechanism is largely reversible or semi-reversible, as the material tends to recover much of its original stiffness upon reloading after unloading-induced softening. Therefore, in this study, "damage" specifically denotes changes in the stress response due to chain rearrangement, rather than irreversible material degradation resulting from chain scission.

3.2.3. Creep and stress relaxation

It is also important to evaluate the creep and stress relaxation behavior of the BeyolexTM film, as these viscoelastic phenomena can affect the long-term performance of stretchable electronic devices. The results of the creep, single-step stress relaxation, and multi-step stress relaxation tests are shown in Fig. 6. The creep and creep recovery tests, presented in Fig. 6(a), were performed by applying a



G

Fig. 3. Isothermal tensile test results for all the temperature considered, (a) strain rate of 0.01 s^{-1} , (b) strain rate of 0.001 s^{-1} , (c) strain rate of 0.0001 s^{-1} (d) comparison at lowest temperature (25 °C) and highest temperature (150 °C).

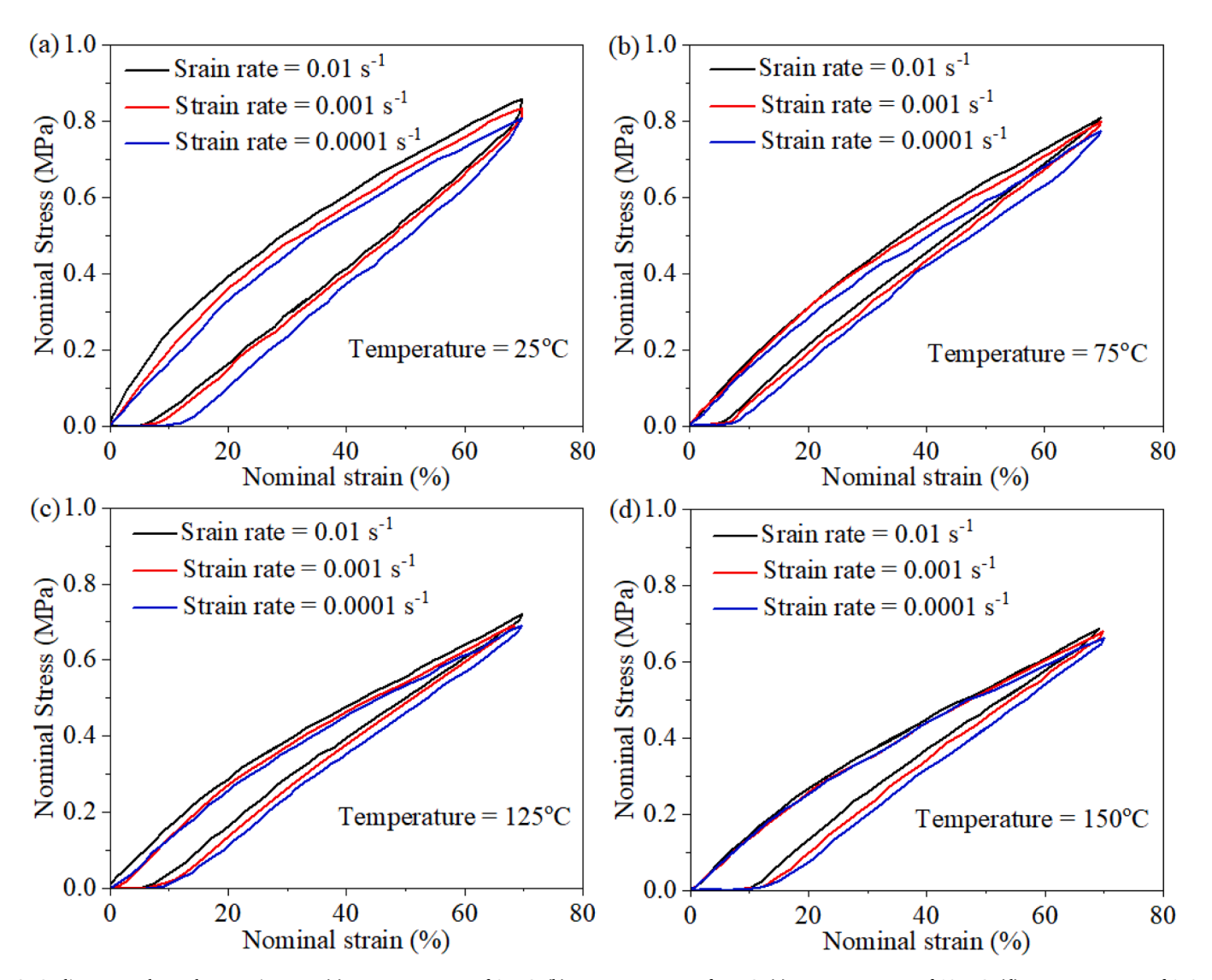


Fig. 4. Cyclic test results at three strain rates, (a) test temperature of 25 °C, (b) test temperature of 75 °C, (c) test temperature of 125 °C, (d) test temperature of 150 °C.

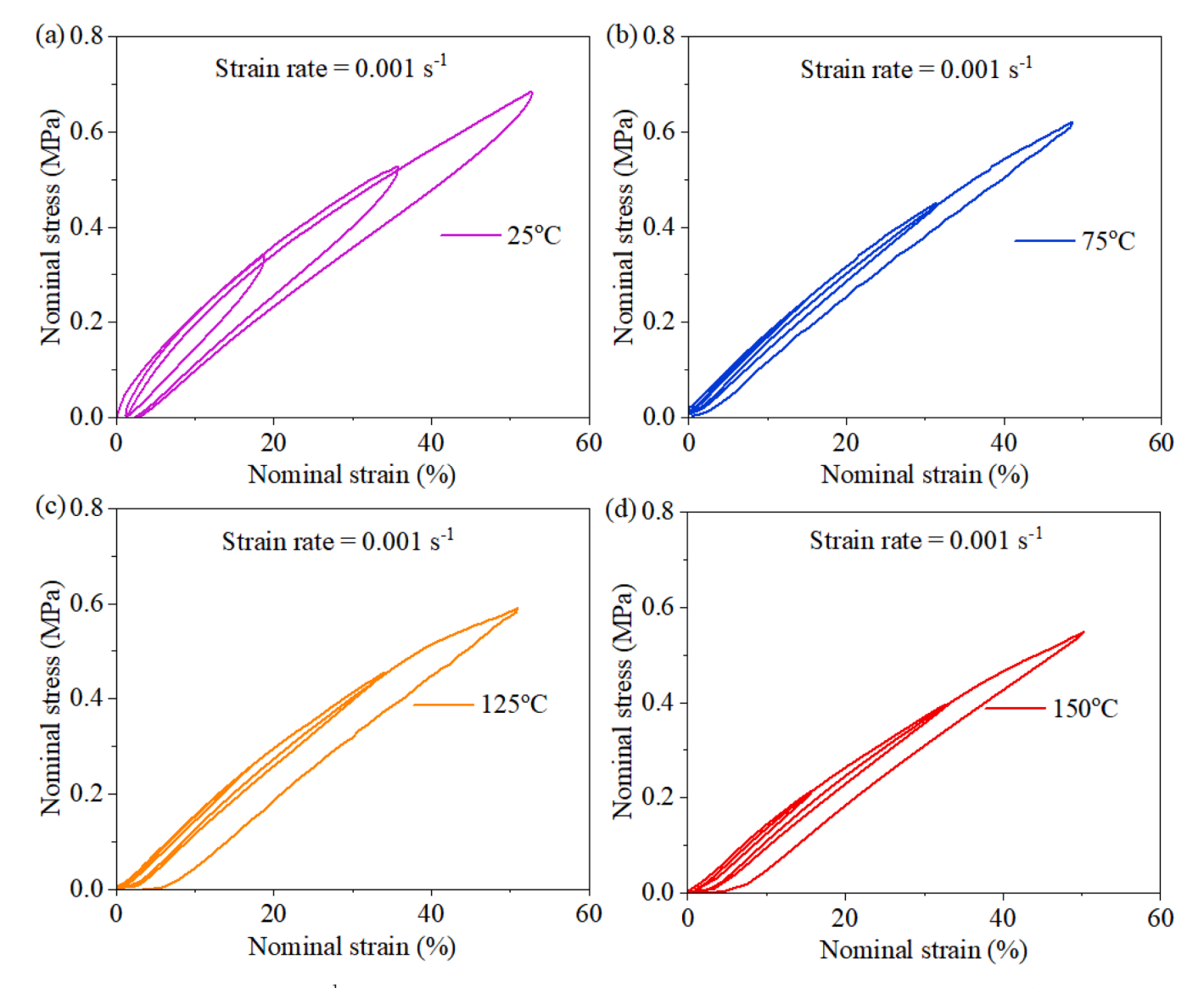


Fig. 5. Step cyclic tests at a strain rate of 0.001 s⁻¹, (a) test temperature of 25 °C, (b) test temperature of 75 °C, (c) test temperature of 125 °C, (d) test temperature of 150 °C.

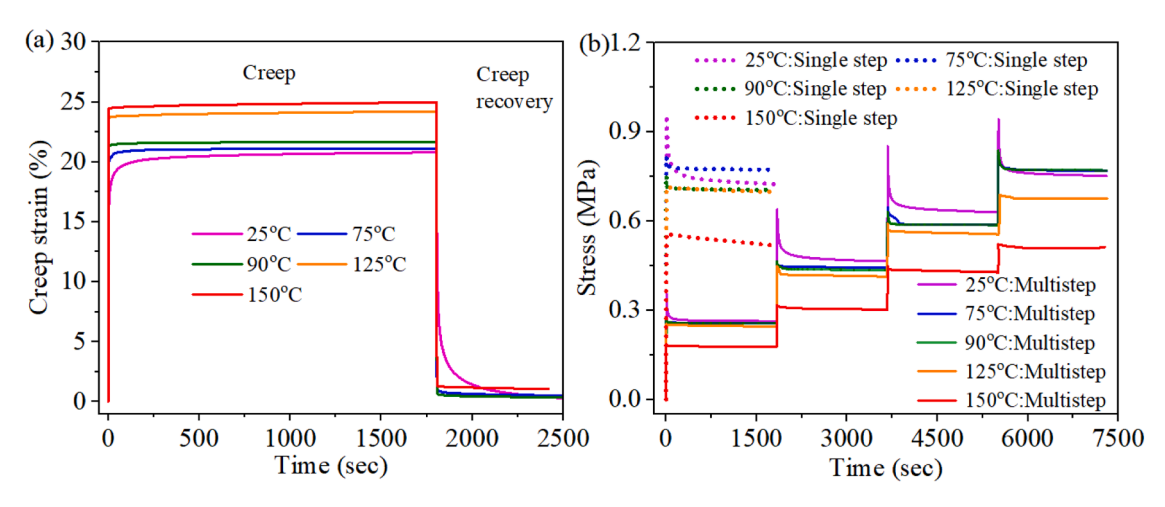


Fig. 6. (a) Creep and creep recovery test results, (b) single and multistep stress relaxation test results.

constant stress of 0.3 MPa to pre-equilibrated samples at the test temperature for 15 min. The creep phase lasted 30 min, after which the stress was removed, and the samples were allowed to recover for an additional 15 min. The time-dependent creep strain trends at elevated temperatures were similar, while the response at room temperature differed. Similarly, the creep recovery behavior was consistent across the higher temperature tests but showed slower strain recovery at 25 °C. This suggests that viscoelastic recovery is more efficient at elevated temperatures, while room temperature conditions lead to a more gradual recovery response.

Soft polymers like the BeyolexTM film are often subjected to single or multi-step strains, during which viscoelastic materials undergo stress relaxation. In the single-step stress relaxation test, a constant strain of 70 % was maintained for 30 min. All samples were preequilibrated for 15 min, similar to the creep test procedure. In the multi-step stress relaxation tests, the same total strain (70 %) was applied incrementally in four steps, with each step followed by a 30-minute relaxation period. Both the single-step and multi-step stress relaxation results are presented in Fig. 6(b). At elevated temperatures, the samples reached their equilibrium stress levels more quickly, with minimal further changes observed during the relaxation period. In contrast, tests conducted at room temperature exhibited a higher level of overstress (defined as the difference between the initial and equilibrium stress). These results indicate that stress relaxation in BeyolexTM is more pronounced at lower temperatures.

4. Thermo-viscoelastic constitutive modeling

Finite strain viscoelasticity extends the theory of linear viscoelasticity, originally developed for infinitesimal strains, to the finite strain regime. For the case of infinitesimal strains, the Cauchy stress tensor for a viscoelastic material (Simo, 1998) is expressed as shown in Eq. (1).

$$\sigma(t) = \int_{-\infty}^{t} b(t-s) \frac{d\sigma_0(s)}{ds} ds$$
 (1)

where σ_0 is the instantaneous stress response of the material and b is the time dependent relative instantaneous relaxation modulus such that,

$$b(t) = b_{\infty} + \sum_{i=1}^{l=n} b_i e^{-\frac{t}{\tau_i}}$$
 (2)

where τ_i is relaxation time of maxwell element i, b_{∞} and b_i are the relative instantaneous stress moduli for spring element and maxwell element i in generalized maxwell model. The values of b_{∞} and b_i are such that $b_{\infty} + \sum_{i=1}^{i=n} b_i = 1$.

For finite strain regime, the deformation gradient **F** is first split into volumetric component $\mathbf{F}^{\mathbf{v}} = J^{\frac{1}{3}}$. **I** and deviatoric component $\mathbf{F}^{\mathbf{d}} = J^{-\frac{1}{3}}$. **F** . Therefore the 2nd Piola Kirchoff stress tensor is given by,

$$\mathbf{S}(\mathbf{C}(t)) = \mathbf{S}^{\mathsf{d}}(\mathbf{C}^{\mathsf{d}}(t)) + \mathbf{S}^{\mathsf{v}}(J(t)) \tag{3}$$

where C^d , C and J are deviatoric Cauchy green deformation tensors, total right Cauchy green deformation tensors and determinant of deformation gradient F.

Ignoring viscous effects in the volumetric stress component, the expression for deviatoric 2nd Piola stress tensor was given in Holzapfel and Simo (1996); Simo (1998) by extending Eq. (1) as,

$$\mathbf{S}^{\mathrm{d}}(t) = 2\mathcal{F}^{\frac{2}{3}} \mathrm{DEV} \left(\int_{-\infty}^{t} b(t-s) \frac{\mathrm{d} \left(\mathrm{DEV} \left(\frac{\partial W_0^{\mathrm{d}}}{\partial \mathbf{c}^{\mathrm{d}}} \right)(s) \right)}{\mathrm{d}s} \right)$$
(4)

where $\text{DEV}([\ .]) = [\ .] - \frac{1}{3} \big([\ .] : \mathbf{C}^d\big) \mathbf{C}^{d^{-1}}$ and W_0^d is the deviatoric component of the material's instantaneous energy function. However, we realized that the instantaneous stress response of the material can be calibrated only if the material has a ceiling to its stress response. This can be found out for the material if the stress response remains stagnant for deformation at increasing loading rates for high strain rate values. Moreover, in pursuit of finding the material's instantaneous stress response, there is a possibility of damaging it. This prompted us to develop a long term or equilibrium stress based integral model within the principles of finite viscoelasticity. For infinitesimal strain linear viscoelasticity model, equilibrium stress-based Cauchy stress tensor for viscoelastic material is given by,

$$\sigma(t) = \int_{-\infty}^{t} g(t-s) \frac{d\sigma_{\infty}(s)}{ds} ds$$
 (5)

where σ_{∞} is the long-term stress response of the material and g is the time dependent relative long term relaxation modulus such that,

$$g(t) = 1 + \sum_{i=1}^{i=n} g_i e^{-\frac{t}{\tau_i}}$$
 (6)

where τ_i and g_i are the relaxation time and relative long term stress modulus for element i. The values of g_i are such that $\sum_{i=1}^{i=n} g_i < 1$. Following the assumption of no viscous effects in the volumetric component of the stress, the deviatoric 2nd Piola stress tensor is extended from Eq. (5) as follows,

$$\mathbf{S}^{\mathrm{d}}(t) = 2 \mathcal{J}^{-\frac{2}{3}} \mathrm{DEV} \left(\int_{-\infty}^{t} g(t-s) \frac{\mathrm{d} \left(\mathrm{DEV} \left(\frac{\partial W_{\mathrm{ob}}^{\mathrm{d}}}{\partial c^{\mathrm{d}}} \right)(s) \right)}{\mathrm{d}s} (s) \, \mathrm{d}s \right)$$
 (7)

where W_{∞}^d is the deviatoric component of the material's equilibrium energy function. Furthermore, this formulation divides the stress response into equilibrium elastic component and viscous component. The temperature effects in the material's stress response can therefore be assessed separately. Eq. (7) is modified to account for temperature related effects as follows,

$$\mathbf{S}^{\mathbf{d}}(t) = 2\mathcal{J}^{-\frac{2}{3}} \text{DEV} \left(\int_{-\infty}^{t'} g(t' - s') \frac{d\left(T_{\theta}(\theta(s))\left(\text{DEV}\left(\frac{\partial W_{\infty}^{\mathbf{d}}}{\partial \mathbf{C}^{\mathbf{d}}}\right)(s)\right)\right)}{ds'} ds' \right)$$
(8)

Such that,

$$ds' = \frac{ds}{H_{\theta}(\theta(s))}$$

$$t' = \int_{-\infty}^{t} \frac{ds}{H_{\theta}(\theta(s))}$$
(9)

where s' and t' are the reduced time variables corresponding to s and t respectively. $T_{\theta}(\theta(s))$ and $H_{\theta}(\theta(s))$ are functions which capture effect of temperature in the material's equilibrium and viscous response separately. $H_{\theta}(\theta(s))$ follows the principle of time-temperature shift functions that are applied in the literature used to capture temperature effect in viscoelastic models.

Now to simplify Eq. (8), we apply integration by part to get,

$$\mathbf{S}^{d}(t) = T_{\theta}(\theta(t))g_{0}\mathbf{S}_{\infty}^{d}(t) + 2J^{-\frac{2}{3}}DEV\left(\int_{-\infty}^{t} \frac{dg(t^{'} - s^{'})}{d(t^{'} - s^{'})}DEV\left(T_{\theta}(\theta(s))\frac{\partial W_{\infty}^{d}}{\partial \mathbf{C}^{d}}(s)\right) ds^{'}\right)$$
(10)

Which simplifies to,

$$\mathbf{S}^{\mathrm{d}}(t) = T_{\theta}(\theta(t)) \mathbf{g}_{0} \mathbf{S}_{\infty}^{\mathrm{d}}(t)$$

$$-2J^{-\frac{2}{3}}DEV\left(\sum_{i=1}^{i=n}\int_{-\tau_{i}}^{t'}\frac{g_{i}}{\tau_{i}}e^{-\frac{(t'-s')}{\tau_{i}}}DEV\left(T_{\theta}(\theta(s))\frac{\partial W_{\infty}^{d}}{\partial \mathbf{C}^{d}}(s)\right)ds'\right)$$
(11)

where $g_0 = g(0) = 1 + \sum_{i=1}^{i=n} g_i$. Applying standard push forward operation, we get

$$au^{d} = \mathbf{F}\mathbf{S}^{d}\mathbf{F}^{T}$$

$$au^{\mathrm{d}} = T_{\mathrm{\theta}}(\theta(t)) g_{\mathrm{0}} au_{\mathrm{m}}^{\mathrm{d}}$$

$$-\operatorname{dev}\left(\sum_{i=1}^{i=n}\int_{-\infty}^{t'} \frac{g_{i}}{\tau_{i}} e^{-\frac{(t'-s')}{\tau_{i}}} T_{\theta}(\theta(s)) \mathbf{F}^{d}(t) \operatorname{DEV}\left(2\frac{\partial W_{\infty}^{d}}{\partial \mathbf{C}^{d}}(s)\right) \mathbf{F}^{d^{T}}(t) \mathrm{d}s'\right)$$

$$(12)$$

where $\text{dev}([.]) = [.] - \frac{1}{3}\text{trace}([.])$ **I** and τ^d is the deviatoric Kirchoff stress tensor. But since the following relation holds,

$$\boldsymbol{\tau}_{\infty}^{d} = \mathbf{F}\mathbf{S}_{\infty}^{d}\mathbf{F}^{T} = 2J^{-\frac{2}{3}}\mathbf{F}\mathbf{DEV}\left(\frac{\partial W_{\infty}^{d}}{\partial \mathbf{C}^{d}}\right)\mathbf{F}^{T} = \mathbf{F}^{d}\mathbf{DEV}\left(2\frac{\partial W_{\infty}^{d}}{\partial \mathbf{C}^{d}}\right)\mathbf{F}^{d^{T}}$$

$$\mathbf{DEV}\left(2\frac{\partial W_{\infty}^{d}}{\partial \mathbf{C}^{d}}\right) = \mathbf{F}^{d^{-1}}\boldsymbol{\tau}_{\infty}^{d}\mathbf{F}^{d^{-T}}$$
(13)

Substituting in Eq. (12) we get,

$$\tau^{\mathrm{d}} = T_{\theta}(\theta(t))g_{0}\tau_{\infty}^{\mathrm{d}}$$

$$-\operatorname{dev}\left(\sum_{i=1}^{i=n}\int_{-\infty}^{t'}\frac{g_{i}}{\tau_{i}}e^{-\frac{(t'-s')}{\tau_{i}}}T_{\theta}(\theta(s)).\mathbf{F}^{d}(t)\mathbf{F}^{d-1}(s)\boldsymbol{\tau}_{\infty}^{d}(s)\mathbf{F}^{d-T}(s)\ \mathbf{F}^{d}(t)\mathrm{d}s'\right)$$

Now since $F^{d}(t)F^{d^{-1}}(s) = F^{d}(s)$ is the relative deviatoric deformation gradient. Therefore Eq. (14) can be written as,

$$\boldsymbol{\tau}^{\mathrm{d}} = T_{\theta}(\theta(t)) \boldsymbol{g}_{0} \boldsymbol{\tau}_{\infty}^{\mathrm{d}}$$

$$-\operatorname{dev}\left(\sum_{i=1}^{i=n}\int_{\tau_{i}}^{t}\frac{g_{i}}{\tau_{i}}e^{-\frac{(t^{'}-s^{'})}{\tau_{i}}}T_{\theta}(\theta(s))\left(\mathbf{F}_{t}^{d}(s)\right)^{-1}\boldsymbol{\tau}_{\infty}^{d}(s)\left(\mathbf{F}_{t}^{d}(s)\right)^{-T}\mathrm{d}s^{'}\right)$$

To capture the stress softening due to damage, Ogden-Roxburgh model (Ogden & Roxburgh, 1999) is incorporated in the equilibrium stress component of the model which is as follows,

$$\tau_{\rm m}^{\rm d} = \eta \tau_{\rm m}^{\rm d}$$
 (16)

where,

$$\eta = 1 - \frac{1}{r} \operatorname{erf} \left(\frac{W_{\text{max}}^{d} - W_{\infty}^{d}}{m + \beta W_{\infty}^{d}} \right) \\
W_{\text{max}}^{d} = \max \left(W_{\infty}^{d}, W_{\text{max}}^{d} \right) \tag{17}$$

where r, m and β are material parameters. When Eq. (17) substituted in Eq. (15), we get

$$\boldsymbol{\tau}^{\mathrm{d}} = \eta(t) T_{\theta}(\theta(t)) g_0 \boldsymbol{\tau}_{\infty}^{\mathrm{d}}$$

$$-\operatorname{dev}\left(\sum_{i=1}^{i=n}\int_{\tau_{i}}^{t'} \frac{g_{i}}{\tau_{i}} e^{-\frac{\left(t'-s'\right)}{\tau_{i}}} T_{\theta}(\theta(s)) \eta(s) \left(\mathbf{F}_{t}^{d}(s)\right)^{-1} \boldsymbol{\tau}_{\infty}^{d}(s) \left(\mathbf{F}_{t}^{d}(s)\right)^{-T} \operatorname{d}s'\right) \right)$$

$$(18)$$

We assume the effects of viscoelasticity and stress softening effects are absent in volumetric component, therefore volumetric Kirchoff Stress becomes,

$$\boldsymbol{\tau}^{\mathbf{v}} = T_{\theta}(\theta(t))\mathbf{F}\mathbf{S}_{\infty}^{\mathbf{v}}\mathbf{F}^{\mathbf{T}} = T_{\theta}(\theta(t))J\frac{\partial U_{\infty}}{\partial J}\mathbf{F}\mathbf{C}^{-1}\mathbf{F}^{\mathbf{T}}$$

$$\boldsymbol{\tau}^{\mathbf{v}}(t) = T_{\theta}(\theta(t))J\frac{\partial U_{\infty}}{\partial J}\mathbf{I} = T_{\theta}(\theta(t))\boldsymbol{\tau}_{\infty}^{\mathbf{v}}$$
(19)

where U_{∞} is the volumetric component of the material's equilibrium energy function. Substituting Eqs. (18) and (19) in Eqn. (20) will give the complete time dependent stress response of the material. Eqn. (20) is as follows,

$$\tau(\mathbf{C}(t)) = \tau^{\mathsf{d}}(\mathbf{C}^{\mathsf{d}}(t)) + \tau^{\mathsf{v}}(J(t)) \tag{20}$$

where τ is the net Kirchoff stress tensor representing the complete stress response of the material at time t.

5. Numerical integration and uniaxial simulation approach

The model represented by Eq. (20) is an integral model where the deviatoric stress has a hereditary integral which requires the history of the material's deformation. For implementation in finite element framework, it is required to simplify the model in such a way that the stress value at current time step can be evaluated using the same at previous time step. As there is no viscosity in the volumetric component of the model, the volumetric stress expression remains the same as given in Eq. (14). For deviatoric stress, we can write Eq. (13) in the following form,

$$\boldsymbol{\tau}^{\mathrm{d}}(t) = \eta(t) T_{\theta}(\theta(t)) g_{0} \boldsymbol{\tau}_{\infty}^{\mathrm{d}} - \operatorname{dev}\left(\sum_{i=1}^{i=n} \boldsymbol{\tau}_{i}^{\mathrm{d}}(t)\right)$$
(21)

where,

$$\boldsymbol{\tau}_{i}^{\mathsf{d}}(t) = \frac{g_{i}}{\tau_{i}} \int_{-\infty}^{t'} \mathrm{e}^{-\frac{(t'-s')}{\tau_{i}}} T_{\theta}(\theta(s)) \eta(s) \left(\mathbf{F}_{t}^{\mathsf{d}}(s)\right)^{-1} \boldsymbol{\tau}_{\infty}^{\mathsf{d}}(s) \left(\mathbf{F}_{t}^{\mathsf{d}}(s)\right)^{-T} \mathrm{d}s'$$

$$(22)$$

Now assuming $\tau_i^{\rm d}(t)$ and $\tau^{\rm d}(t)$ are known. Therefore, considering dt as a small increment forward in time, the expression $\tau_i^{\rm d}$ for $t+{\rm d}t$,

$$\boldsymbol{\tau}_{i}^{\mathrm{d}}(t+\mathrm{d}t) = \frac{g_{\mathrm{I}}}{\tau_{i}} \int_{-\infty}^{t'+\mathrm{d}t'} \mathrm{e}^{-\frac{(t'+\mathrm{d}t'-s')}{\tau_{i}}} T_{\theta}(\theta(s)) \eta(s) \left(\mathbf{F}_{t+\mathrm{d}t}^{\mathrm{d}}(s)\right)^{-1} \boldsymbol{\tau}_{\infty}^{\mathrm{d}}(s) \left(\mathbf{F}_{t+\mathrm{d}t}^{\mathrm{d}}(s)\right)^{-T} \mathrm{d}s'$$

$$\mathrm{d}t' = \frac{\mathrm{d}t}{H_{\theta}(\theta(s))}$$
(23)

If $\Delta \mathbf{F}^d$ is the increment in deviatoric deformation gradient tensor such that $\Delta \mathbf{F}^d = \mathbf{F}^d(t+dt) \left(\mathbf{F}^d(t)\right)^{-1}$, therefore $\mathbf{F}^d_{t+dt}(s)$ in Eq. (23) can be written as,

$$\mathbf{F}_{r,dr}^{d}(s) = \mathbf{F}_{r}^{d}(s) \left(\Delta \mathbf{F}^{d}\right)^{-1} \tag{24}$$

We can split the integral between $-\infty$ to t and t to t+dt and substitute Eq. (24) as follows,

$$\tau_{i}^{d}(t+dt) = \Delta \mathbf{F}^{d} e^{-\frac{dt'}{\tau_{i}}} \underbrace{g_{i}}_{\tau_{i}} \left(\int_{-\infty}^{t'} e^{-\frac{(t'-s')}{\tau_{i}}} T_{\theta}(\theta(s)) \eta(s) \left(\mathbf{F}_{t}^{d}(s)\right)^{-1} \boldsymbol{\tau}_{\infty}^{d}(s) \left(\mathbf{F}_{t}^{d}(s)\right)^{-T} ds' \right) \Delta \mathbf{F}^{d^{T}} \\
+ \underbrace{g_{i}}_{\tau_{i}} \int_{t'}^{t'+dt'} e^{-\frac{(t'+dt'-s')}{\tau_{i}}} T_{\theta}(\theta(s)) \eta(s) \left(\mathbf{F}_{t+dt}^{d}(s)\right)^{-1} \boldsymbol{\tau}_{\infty}^{d}(s) \left(\mathbf{F}_{t+dt}^{d}(s)\right)^{-T} ds'$$
(25)

The first term has the same expression as $\tau_i^d(t)$. We simplify the second term by considering the product $\left(\mathbf{F}_{t+\mathrm{d}t}^d(s)\right)^{-1}\tau_\infty^d(s)\left(\mathbf{F}_{t+\mathrm{d}t}^d(s)\right)^{-T}$ to be linear between that at t and t+dt. The linear relation is as follows,

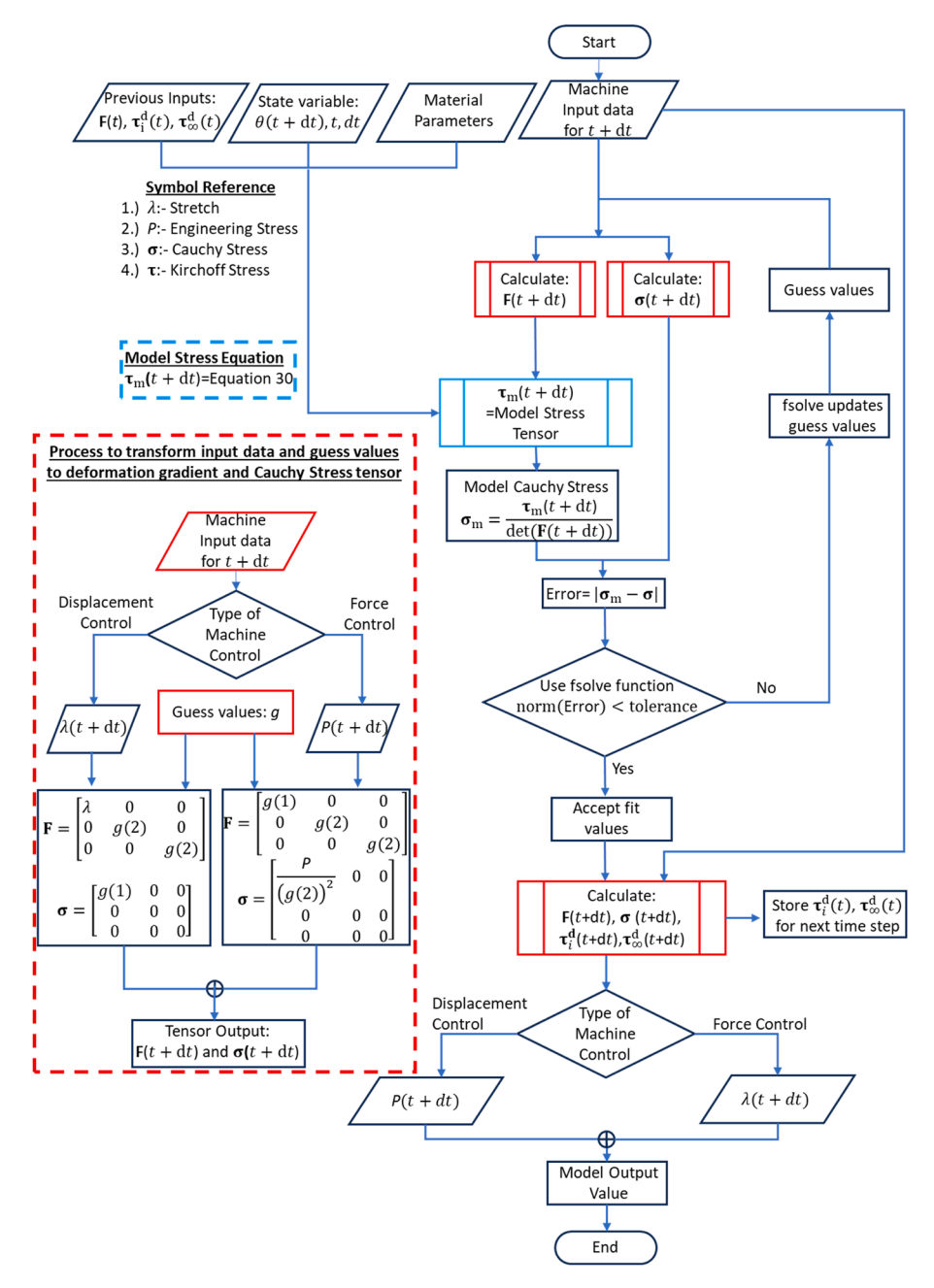


Fig. 7. Algorithm to calculate model engineering stress or stretch output based on machine input.

$$\operatorname{at} s' = t', \left(\mathbf{F}_{t+\mathrm{d}t}^{\mathrm{d}}(t)\right)^{-1} \boldsymbol{\tau}_{\infty}^{\mathrm{d}}(t) \left(\mathbf{F}_{t+\mathrm{d}t}^{\mathrm{d}}(t)\right)^{-T} = \Delta \mathbf{F}^{\mathrm{d}} \boldsymbol{\tau}_{\infty}^{\mathrm{d}}(t) \Delta \mathbf{F}^{\mathrm{d}^{\mathrm{T}}}$$

$$\operatorname{at} s' = t' + dt', \left(\mathbf{F}_{t+\mathrm{d}t}^{\mathrm{d}}(t+\mathrm{d}t)\right)^{-1} \boldsymbol{\tau}_{\infty}^{\mathrm{d}}(t+\mathrm{d}t) \left(\mathbf{F}_{t+\mathrm{d}t}^{\mathrm{d}}(t+\mathrm{d}t)\right)^{-T} = \boldsymbol{\tau}_{\infty}^{\mathrm{d}}(t+\mathrm{d}t)$$

$$\left(\mathbf{F}_{t+\mathrm{d}t}^{\mathrm{d}}(s)\right)^{-1} \boldsymbol{\tau}_{\infty}^{\mathrm{d}}(s) \left(\mathbf{F}_{t+\mathrm{d}t}^{\mathrm{d}}(s)\right)^{-T} = \frac{(t'+dt'-s')}{\mathrm{d}t'} \left(\Delta \mathbf{F}^{\mathrm{d}} \boldsymbol{\tau}_{\infty}^{\mathrm{d}}(t) \Delta \mathbf{F}^{\mathrm{d}^{\mathrm{T}}}\right) + \frac{s'-t'}{\mathrm{d}t'} \left(\boldsymbol{\tau}_{\infty}^{\mathrm{d}}(t+\mathrm{d}t)\right)$$

$$(26)$$

After substituting Eq. (22) in Eq. (25) and integrating the second term by substituting Eq. (26) in Eq. (25), after simplification we get,

$$\tau_{i}^{d}(t+dt) = \Delta \mathbf{F}^{d} e^{-\frac{dt}{\tau_{i}}} \tau_{i}^{d}(t) \Delta \mathbf{F}^{d^{T}}
+ g_{i} \left(T_{\theta}(\theta(t)) \eta(t) \Delta \mathbf{F}^{d} \tau_{\infty}^{d}(t) \Delta \mathbf{F}^{d^{T}} \cdot \left(\frac{\tau_{i}}{dt'} - \left(1 + \frac{\tau_{i}}{dt'} \right) e^{-\frac{dt'}{\tau_{i}}} \right) \right)
+ g_{i} \left(T_{\theta}(\theta(t+dt)) \eta(t+dt) \tau_{\infty}^{d}(t+dt) \cdot \left(1 - \frac{\tau_{i}}{dt'} + \frac{\tau_{i}}{dt'} e^{-\frac{dt'}{\tau_{i}}} \right) \right)$$
(27)

This equation can be further simplified as,

$$\tau_i^{d}(t+dt) = e^{-\frac{dt}{\tau_i}} \Delta \mathbf{F}^{d} \tau_i^{d}(t) \Delta \mathbf{F}^{d^{\mathrm{T}}} + g_i A_i T_{\theta}(\theta(t)) \eta(t) \Delta \mathbf{F}^{d} \tau_{\infty}^{d}(t) \Delta \mathbf{F}^{d^{\mathrm{T}}}
+ g_i B_i T_{\theta}(\theta(t+dt)) \eta(t+dt) \tau_{\infty}^{d}(t+dt)$$
(28)

Where.

$$A_{i} = \frac{\tau_{i}}{dt'} - \left(1 + \frac{\tau_{i}}{dt'}\right) e^{-\frac{dt'}{\tau_{i}}}$$

$$B_{i} = 1 - \frac{\tau_{i}}{dt'} + \frac{\tau_{i}}{dt'} e^{-\frac{dt'}{\tau_{i}}}$$

$$(29)$$

Based on Eq. (20), total Kirchoff stress is given by,

$$\tau(t+dt) = T_{\theta}(\theta(t+dt))\tau_{\infty}^{v}(t+dt) + \eta(t+dt)T_{\theta}(\theta(t+dt))g_{0}\tau_{\infty}^{d}(t+dt) - \operatorname{dev}\left(\sum_{i=1}^{i=n}\tau_{i}^{d}(t+dt)\right)$$
(30)

Eq. (30) represents the material's time-dependent stress response at time t+dt. Evaluating this response requires the equilibrium volumetric and deviatoric stress tensor values at t+dt as well as the deformation gradient tensor F, the deviatoric Kirchhoff stress tensor of Maxwell element i, and the equilibrium deviatoric stress tensor from the previous time step t. We designed the model equation to evaluate the output for both displacement-controlled input in the form of stretch λ and force-controlled input in the form of engineering stress P. Multi-rate tensile tests, single-step and multi-step relaxation tests, and cyclic tests are all displacement-controlled, where the stretch λ , along with time and temperature (as provided by the testing machine), are input to compute the true or engineering stress during the experiment. In contrast, the creep test is a force-controlled test, where the input is the applied force expressed as engineering stress *P* at the corresponding time and temperature. The goal in this case is to evaluate the evolution of strain or stretch in the specimen over time. Additionally, since the material is not assumed to be incompressible, Eq. (30) does not directly yield the Kirchhoff stress tensor. To construct the full deformation gradient tensor under uniaxial loading, stretch values are required in both the axial and transverse directions. While uniaxial tests provide the axial stretch, the transverse stretch is treated as an additional model output. Due to these considerations, we developed an iterative root-finding numerical algorithm—illustrated in Fig. 7—that evaluates the model's response based on the type of machine input. The algorithm is designed to compute the model response at time t+dt based on the corresponding machine input. The initial guess values used to construct the deformation gradient tensor F and Cauchy stress tensor σ depend on the loading type (uniaxial in this case) and type of machine input (displacement controlled or force controlled). These guess values are initialized to 1 for stretch components and 0 for stress components. Otherwise, guess values at time t+dt are taken as fit values for time t. The constructed deformation gradient tensor is then used to evaluate the model's Kirchhoff stress tensor. This tensor is subsequently transformed into the Cauchy stress tensor and subtracted from the constructed Cauchy stress tensor to form an error vector, as illustrated in the algorithm (Fig. 7). The norm of this error vector is minimized using MATLAB's fsolve function, which iteratively updates the guess values. The solution is accepted once the error norm falls below a tolerance of 10⁻⁸. The final fitted values are used to construct final deformation gradient and Cauchy stress tensor as an output from the model. These tensors are later used to give engineering stress value as an output if the loading was displacement controlled and stretch value if the same was force controlled. This algorithm enables fast computation of model outputs, allows flexibility in choosing different equilibrium stress models, and removes the need to derive stretch-based equations for uniaxial loading. Furthermore, it can be adjusted to simulate model response for other loading types, including equibiaxial, shear, and volumetric loading. Fig. 7 illustrates the corresponding numerical algorithm used to compute the model-predicted engineering stress or stretch based on the machine input conditions.

6. Material parameter identification and validation

The finite viscoelastic model formulated so as to distinguish different aspects of material's stress response for ease in its calibration. The model as described in Section 4 comprises of equilibrium and viscous components. The temperature effects are also distinguished in both the components of the material. This makes it easier to compartmentalize the material's stress response and then calibrate the part of the model which captures that. The following sections will clarify the utility of the different components of the model and the ease in their material parameter calibration.

6.1. Elastic parameter identification

Equilibrium response of a viscoelastic material can be found out in 2 ways. When the material is deformed at a very slow strain rate, the component of material's viscosity on its stress response becomes negligible. It is also termed as quasi-static response of the material. Quasistatic rate of deformation is experimentally impossible since theoretically it will take large amount of time. However, deforming at a very slow rate achieves the same result given that decreasing the deformation rate any further does not decrease the stress response. Moreover, there is another way to discern a material's equilibrium response. By conducting single-step or multi-step relaxation tests, one can observe the relaxed stress values against the final deformed strain values. Once the material is held at constant strain after deformation at high strain rates, it relaxes to its equilibrium value. These equilibrium stress values at respective strains are independent of material's inherent viscosity. By juxtaposing the relaxed equilibrium and quasistatic slow rate stress values obtained at 25 °C for Beyolex as shown in Fig. 7, one can observe the equilibrium response of the material. We found reduced polynomial model of degree 2 energy function sufficient enough to capture the equilibrium response.

$$W_{\infty}(\mathbf{C}) = W_{\infty}^{d}(\mathbf{C}^{d}) + U_{\infty}(J)$$

$$W_{\infty}(\mathbf{C}) = C_{10}(I_{1}^{d} - 3) + C_{20}(I_{1}^{d} - 3)^{2} + \frac{1}{D_{1}}(J - 1)^{2} + \frac{1}{D_{2}}(J - 1)^{4}$$

$$\boldsymbol{\tau}_{\infty}^{d} = 2(C_{10} + 2C_{20}(I_{1}^{d} - 3))\operatorname{dev}(\mathbf{B}^{d})$$

$$\boldsymbol{\tau}_{\infty}^{v} = 2J\left(\frac{1}{D_{1}}(J - 1) + \frac{2}{D_{2}}(J - 1)^{3}\right)\mathbf{I}$$

$$\boldsymbol{\tau}_{\infty} = \boldsymbol{\tau}_{\infty}^{d} + \boldsymbol{\tau}_{\infty}^{v}$$
(31)

where I_1^d is first invariant of deviatoric right Cauchy green deformation tensor \mathbf{C}^d . We applied uniaxial loading condition to the Kirchoff stress tensor and calculated engineering stress tensor and calibrated the constants to capture the Beyolex's equilibrium engineering stress response. The calibrated values are $C_{10}=0.342$ MPa, $C_{20}=0.00893$ MPa, $D_1=1.318$ MPa⁻¹ and $D_2=1.818$ MPa⁻¹ and the fit is shown in Fig. 8.

6.2. Viscous parameter calibration

Section 6.1 fixed the values of parameters responsible for equilibrium stress response for BeyolexTM. Viscous stress response manifests when the material is deformed at different loading rates, stress relaxation and creep loading histories. Therefore, Prony series values τ_i and g_i which are responsible for Beyolex's viscoelastic response will be calibrated using the aforementioned experimental tests. We used lsqcurvefit function in MATLAB to optimize the viscous material parameters to model algorithm displayed in Fig. 7 to simulate the experimental output. Upon repeated trials, we found that 3 terms of Prony series were enough to capture the viscoelastic response of Beyolex at 25 °C. Uniqueness of the algorithm allowed calibration of the viscous model parameters using force-controlled test like creep along with displacement-controlled tests like stress relaxation together. The values of the constants are displayed in Table 1 and the model results against experimental outputs are displayed in Fig. 9.

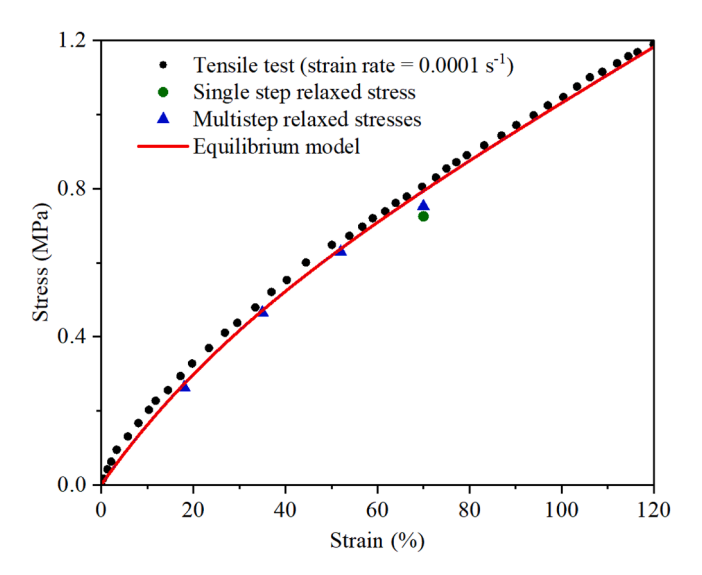


Fig. 8. Equilibrium stress model comparison with slow rate and relaxed stress values.

Table 1
Viscous parameter values.

Relative stress modulus	Values	Relaxation time	Values (seconds)
g ₁	0.0008	$ au_1$	19.06
g_2	0.329	$ au_2$	13.7
g ₃	0.0265	$ au_3$	1800.55

6.3. Temperature scaling parameter identification

Until now, the equilibrium and viscous response of the Beyolex is captured for 25 °C. However, to capture its response due to temperature, the formulation is done so as to assess it in its equilibrium and viscous component. The effect of the increase in temperature in Beyolex's equilibrium response was discerned by observing the slow rate tensile data for each temperature as shown in Fig. 10.

We find that the equilibrium stress softens as temperature increases. We capture this effect using the following function that when multiplied to the equilibrium stress captures the effect of an increase in temperature.

$$T_{\theta}(\theta) = 1 - R_{1}(\theta - \theta_{\text{ref}}) \tag{32}$$

where R_1 is a material parameter and θ_{ref} is a reference temperature which in this case is 25 °C. We found Eq. (32) sufficient to capture the equilibrium stress softening due to temperature. The comparison of the temperature incorporated equilibrium stress model with respective slow rate data is shown in Fig. 10 and the value of the material parameter R_1 was found to be 0.0013°C⁻¹

After capturing the effect of temperature in material's equilibrium response, we observed how temperature had an effect on Beyolex's viscosity. We found that as temperature is increased, the material transits from viscoelasticity to near perfect elasticity. This is observed in relaxation and creep data as well. Therefore, the principle of time-temperature shift function is applied in the formulation as shown in Eq. (9). We found that a linear function in logarithm was sufficient to capture this effect.

$$-\log_{10}H_{\theta}(\theta) = R_2(\theta - \theta_{\text{ref}})^n \tag{33}$$

Incorporating Eq. (33) in Eq. (9) and running a calibration for temperature data for 0.01/s and 0.001/s strain rate loading, we found it sufficient enough to capture the temperature effect. The results are displayed in Fig. 11 and the temperature function parameters identified are $R_2 = 0.289$, n = 0.4.

6.4. Damage parameter identification

Upon using the model for cyclic loading, it was observed that the stress softening due to viscoelasticity was insufficient to capture the hysteresis. The stress softening during unloading was found to be contributed to by damage as well during loading. We therefore used the modification to the model done in Eq. (16). We calibrated the Ogden-Roxborogh model constants using the data for cyclic and step cyclic tests performed at 0.001 s strain rate. We found the modification sufficient for the model to capture the stress softening effects as displayed by Fig. 12. The values of the constants are r = 1, m = 0.73 and $\beta = 3 \times 10^{-14}$.

6.5. Model validation

In the previous sections, we used different aspects of materials deformation behavior to calibrate different parts of the model. But to verify the validity of the model, we wished to test the model under different loading histories across different temperatures. From the experiments it was observed that the material changes its stress-deformation relationship from viscoelasticity to near elasticity when temperature is increased from room temperature to 150 °C. We attempted to capture this temperature effect in our model which we wished to simulate using creep and relaxation loading histories for 75 °C, 90 °C and 125 °C. These temperatures also fall under the operational temperature of devices made from Beyolex material. As illustrated in Fig. 13, the model adequately simulates creep, single-step, and multi-step relaxation loading histories across the aforementioned temperature conditions. Furthermore, applications concerning Beyolex material also experience cyclic loads in the operational temperature range. Therefore, we simulated the uniaxial loading in step-cyclic and different loading rate cyclic strain histories for 75 °C, 90 °C and 125 °C. The results are as displayed in Fig. 14. The model adequately captures the stress softening resulting from hysteresis during cyclic loading at higher temperatures.

7. Conclusions

This study presents a comprehensive experimental characterization of BeyolexTM, a non-silicone thermoset polymer used in stretchable electronics, under realistic thermal and mechanical loading conditions. Thermal analysis confirmed a degradation onset near 270 °C, validating that the selected operational temperature range is safe. Mechanical testing demonstrated a transition from viscoelastic to nearly elastic behavior with increasing temperature, as seen in multi-rate tensile, creep, and stress relaxation tests. A finite viscoelastic integral model was proposed to capture Beyolex's combined hyperelastic, viscoelastic, thermal, and stress-softening responses. A root-finding algorithm was developed to simulate model output based on machine input type (force- or displacement-

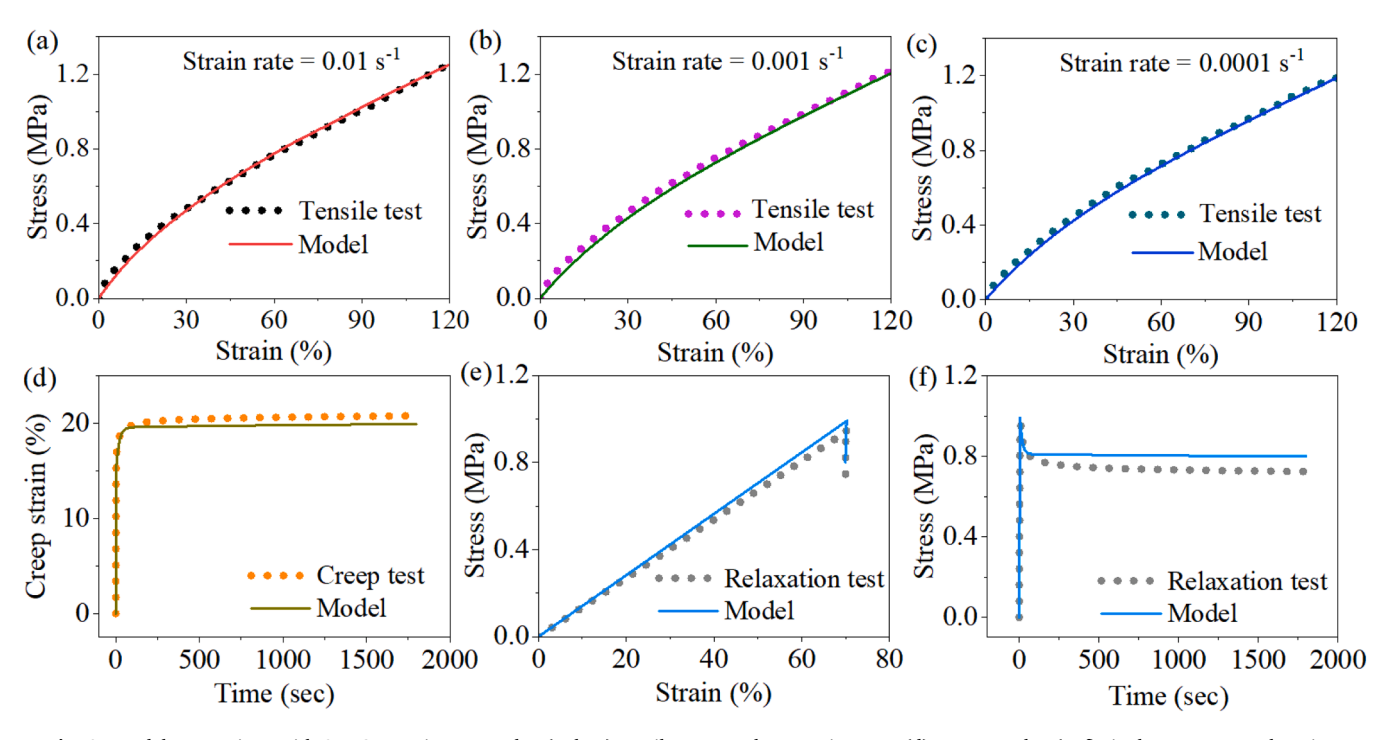


Fig. 9. Model comparison with 25 °C experiment results, (a, b, c) tensile tests at three strain rates, (d) creep results, (e, f) single step stress relaxation.

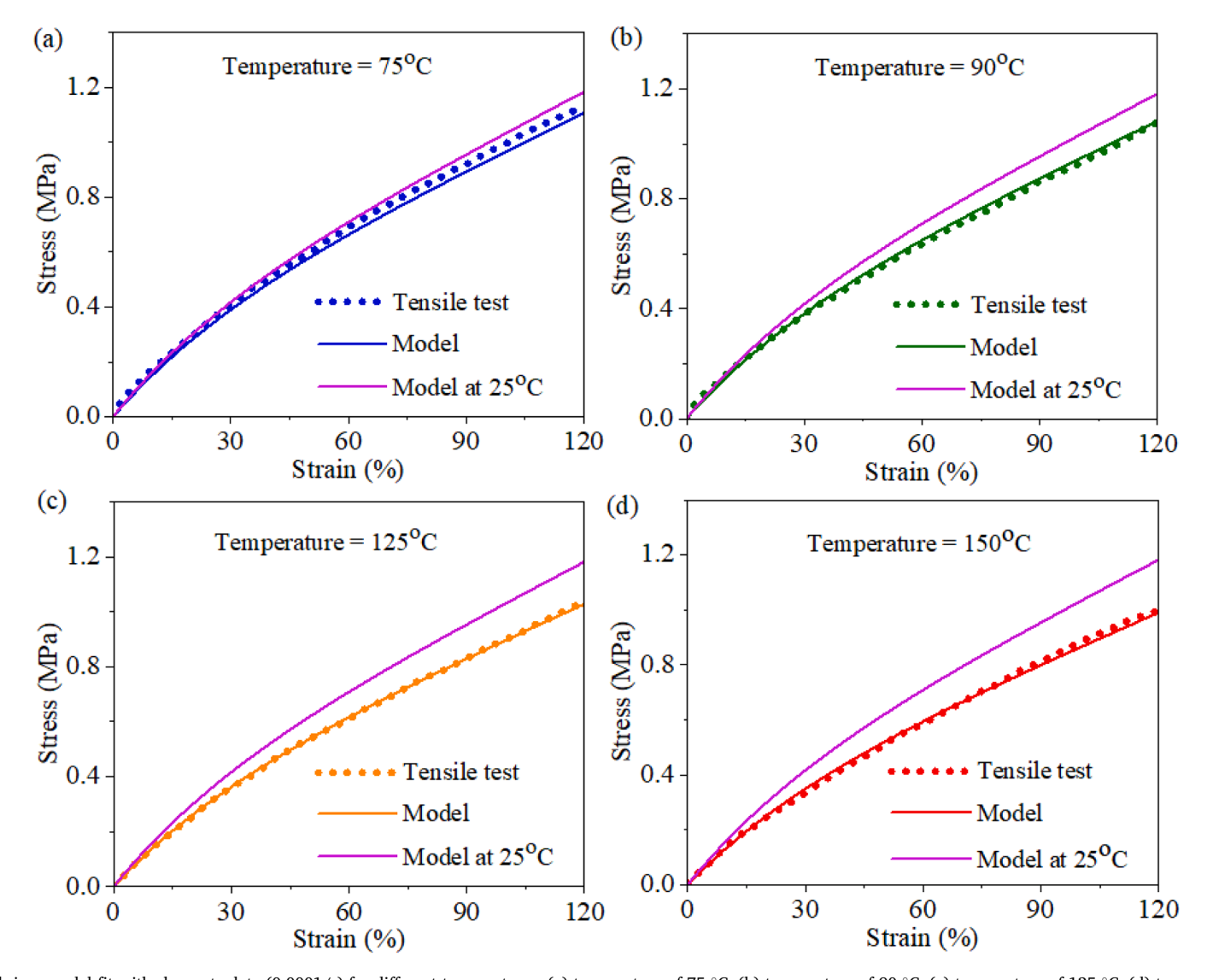


Fig. 10. Equilibrium model fit with slow rate data (0.0001/s) for different temperatures, (a) temperature of 75 °C, (b) temperature of 90 °C, (c) temperature of 125 °C, (d) temperature of 150 °C.

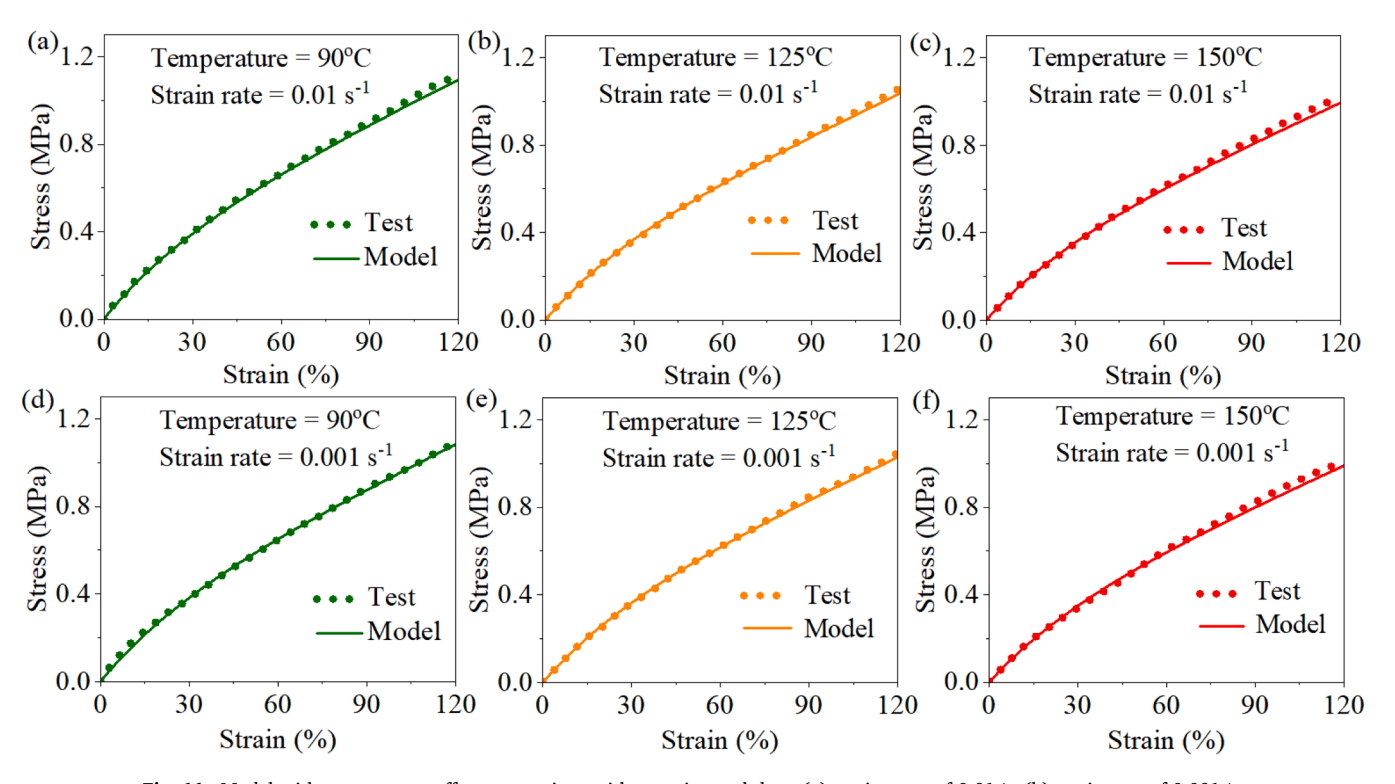


Fig. 11. Model with temperature effect comparison with experimental data, (a) strain rates of 0.01/s, (b) strain rate of 0.001/s.

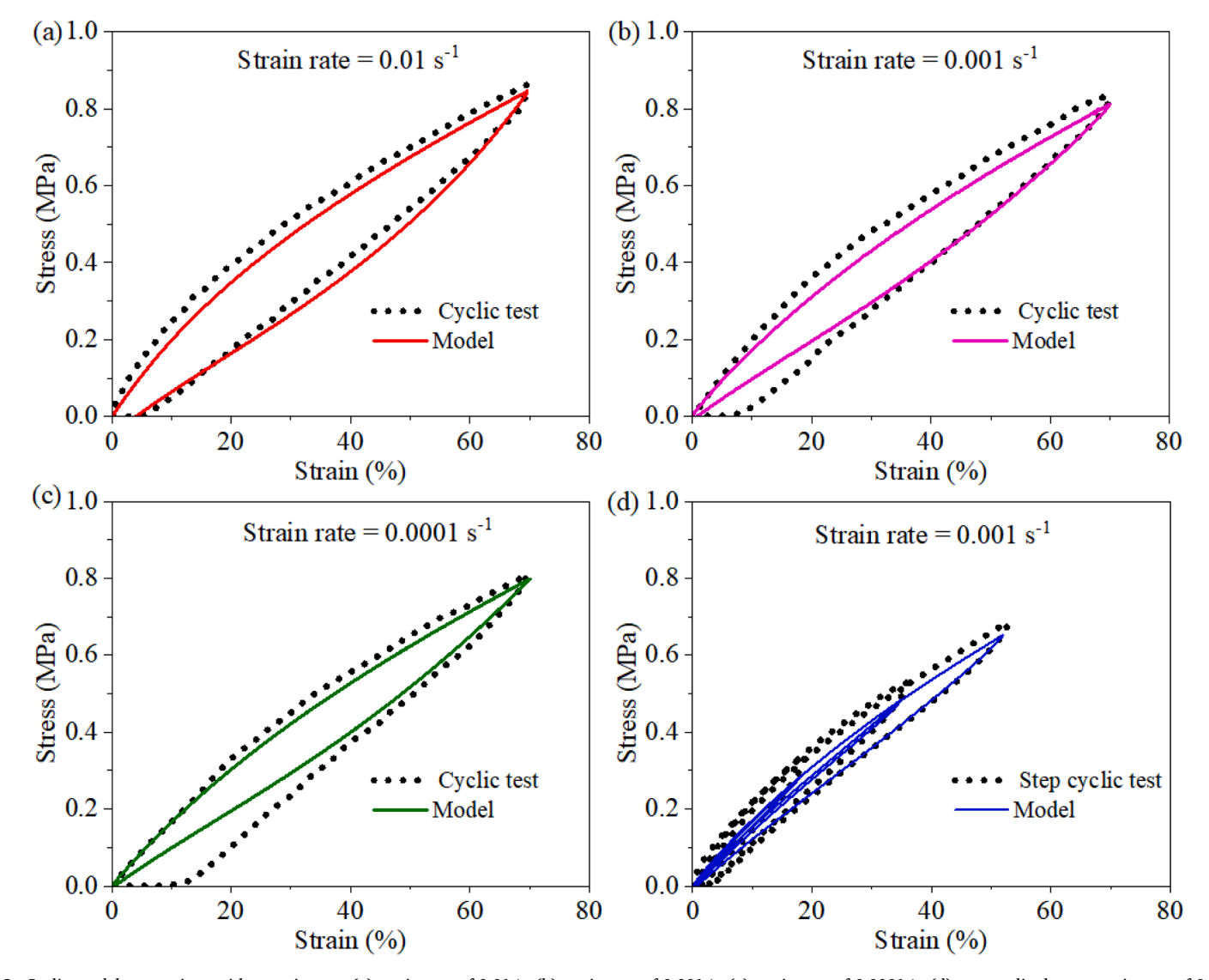


Fig. 12. Cyclic model comparison with experiments, (a) strain rate of 0.01/s, (b) strain rate of 0.001/s, (c) strain rate of 0.0001/s, (d) step cyclic data at strain rate of 0.001/s.

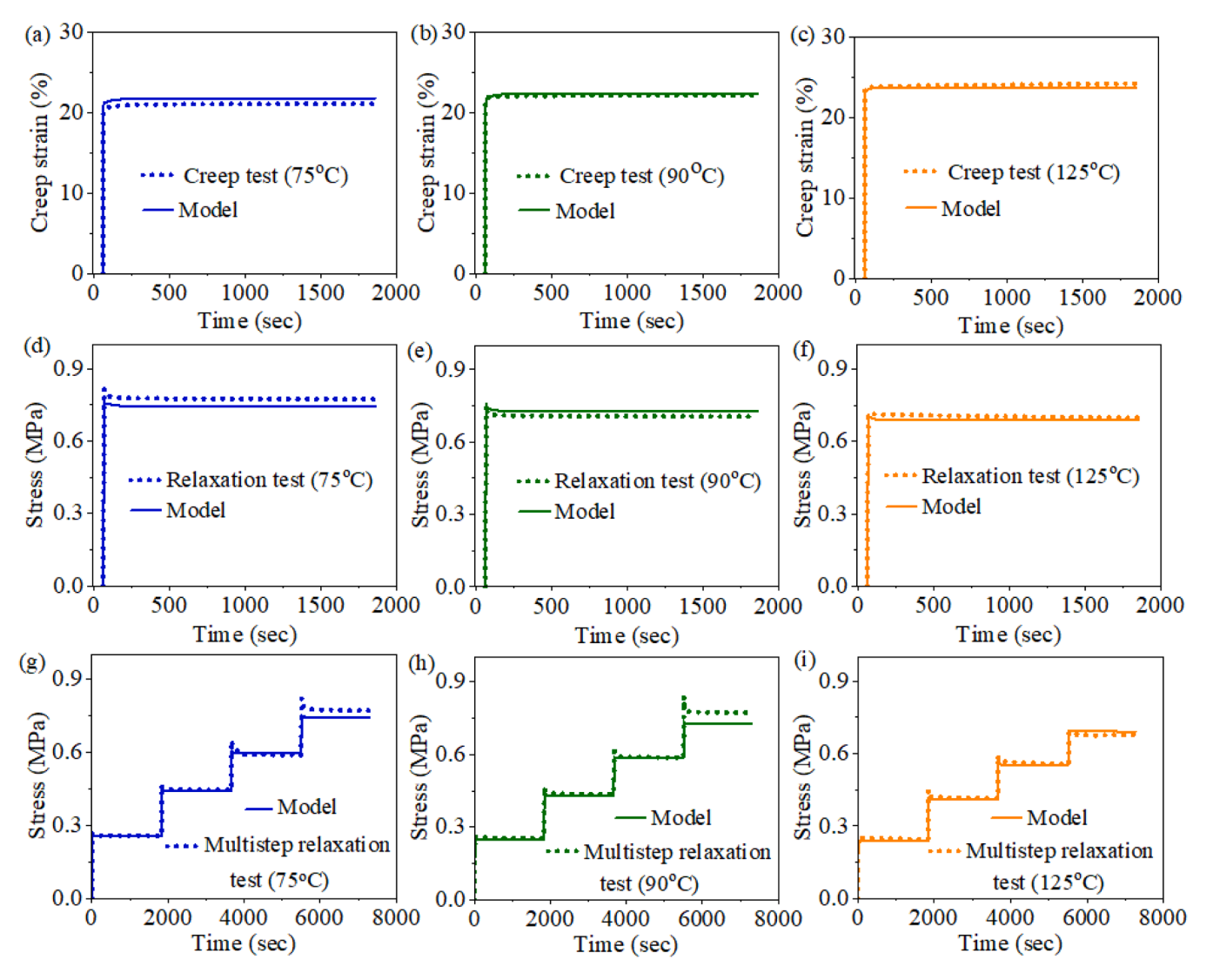


Fig. 13. (a, b, c) creep results, (d, e, f) stress relaxation results, (g, h, i) multistep stress relaxation results.

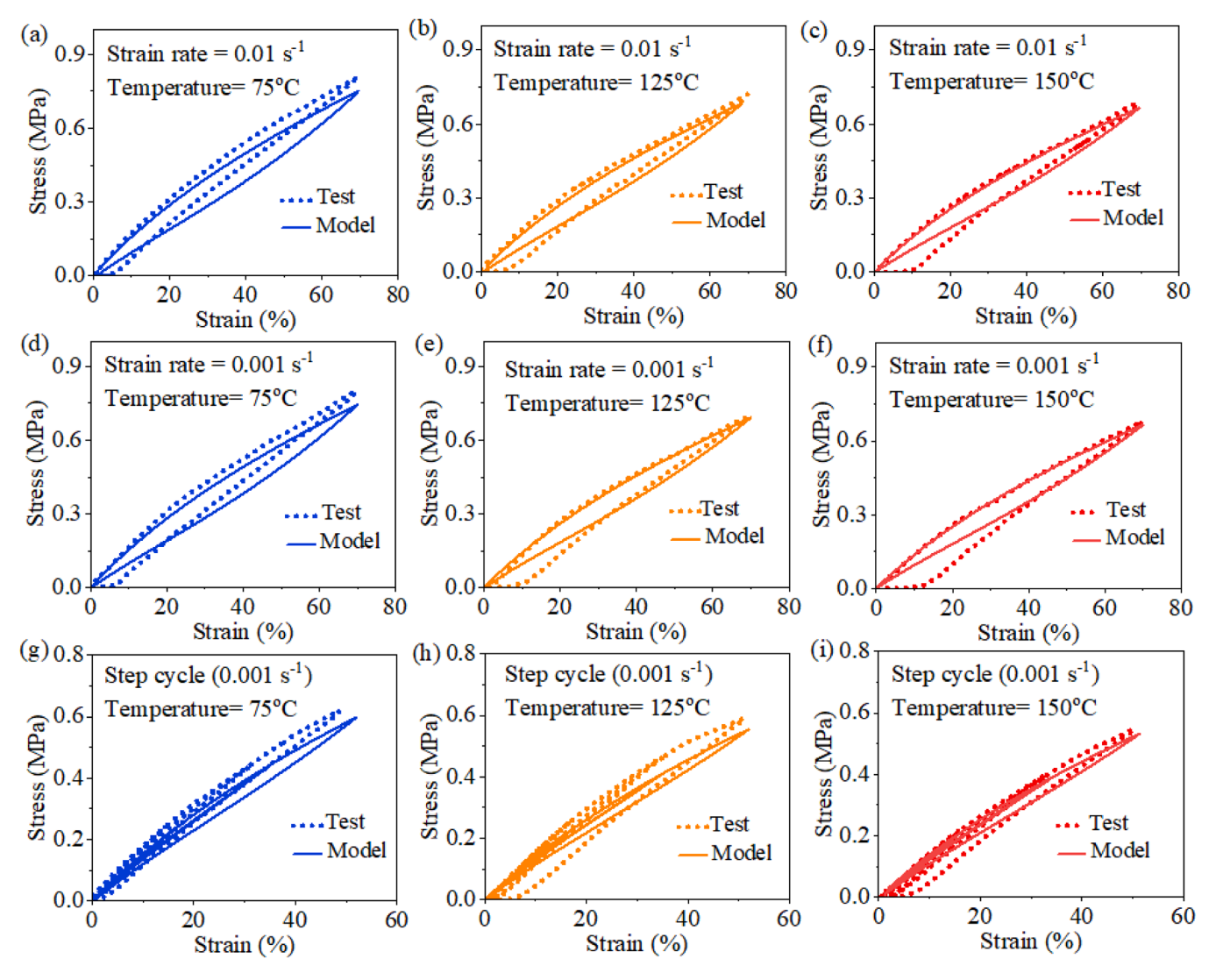


Fig. 14. Model comparison with experimental results, (a,b,c) cyclic results at strain rate of 0.01/s for temperature of 75 °C, 125 °C and 150 °C, (d, e ,f) cyclic results at strain rate of 0.001/s for temperature of 75 °C, 125 °C and 150 °C, (g, h, i) step-cyclic results at strain rate of 0.001/s for temperature of 75 °C, 125 °C and 150 °C.

controlled), directly in tensor form—eliminating the need for manual derivation of stretch-based equations and reducing potential

The model structure allows systematic, stepwise calibration and shows strong agreement with experimental data across various loading histories. However, the model only approximated stress retention during multi-step relaxation tests, indicating a need for improved viscoelastic modeling in such cases. Additionally, the current model lacks a fatigue component, which is critical for real-world cyclic loading scenarios. Future work will focus on investigating the fatigue behavior of BeyolexTM and extending testing to multiaxial loading conditions.

CRediT authorship contribution statement

Siddhesh S. Kulkarni: Writing – original draft, Visualization, Validation, Software, Methodology, Investigation, Data curation, Conceptualization. Israr Ud Din: Writing – original draft, Visualization, Software, Resources, Methodology, Investigation, Formal analysis, Data curation, Conceptualization. Yarjan Abdul Samad: Writing – review & editing, Resources. Kamran A. Khan: Writing – review & editing, Supervision, Resources, Project administration, Methodology, Investigation, Funding acquisition, Conceptualization.

Declaration of competing interest

The authors declare that they have no known competing financial interests or personal relationships that could have appeared to influence the work reported in this paper.

Data availability

Data will be made available on request.

References

- Ahmed, A., Din, I. U., Kulkarni, S., & Khan, K. A. (2024). Multiscale finite element modeling of origami-inspired dual matrix deployable composite with viscohyperelastic hinge. Composite Structures, 343. Article 118301.
- Amjadi, M., Yoon, Y. J., & Park, I. (2015). Ultra-stretchable and skin-mountable strain sensors using carbon nanotubes–Ecoflex nanocomposites. *Nanotechnology*, 26, Article 375501. https://doi.org/10.1088/0957-4484/26/37/375501
- Arruda, E. M., & Boyce, M. C. (1993). A three-dimensional constitutive model for the large stretch behavior of rubber elastic materials. *Journal of the Mechanics and Physics of Solids*, 41, 389–412. https://doi.org/10.1016/0022-5096(93)90013-6
- Bergstrom, J. (1998). Constitutive modeling of the large strain time-dependent behavior of elastomers. *Journal of the Mechanics and Physics of Solids*, 46, 931–954. https://doi.org/10.1016/S0022-5096(97)00075-6
- Bernstein, B., Kearsley, E. A., & Zapas, L. J. (1963). A study of stress relaxation with finite strain. *Transactions of the Society of Rheology*, 7, 391–410. https://doi.org/10.1122/1.548963
- Bucchi, A., De Tommasi, D., Puglisi, G., & Saccomandi, G. (2023). Damage as a material phase transition. *Journal Of Elasticity*, 154, 325–344. https://doi.org/
- Eckart, C. (1940). The thermodynamics of irreversible processes. III. Relativistic theory of the simple fluid. *The Physical review*, 58, 919–924. https://doi.org/10.1103/PhysRev.58.919
- Fan, J. A., Yeo, W.-H., Su, Y., Hattori, Y., Lee, W., Jung, S.-Y., Zhang, Y., Liu, Z., Cheng, H., Falgout, L., Bajema, M., Coleman, T., Gregoire, D., Larsen, R. J., Huang, Y., & Rogers, J. A. (2014). Fractal design concepts for stretchable electronics. *Nature Communications*, 5, 3266. https://doi.org/10.1038/ncomms4266
- Fung, Y. C. (1993). Mechanics of erythrocytes, leukocytes, and other cells. Biomechanics (pp. 109–164). New York, NY: Springer New York. https://doi.org/10.1007/978-1-4757-2257-4_4
- Holzapfel, G. A., & Simo, J. C. (1996). A new viscoelastic constitutive model for continuous media at finite thermomechanical changes. *International Journal of Solids and Structures*, 33, 3019–3034. https://doi.org/10.1016/0020-7683(95)00263-4
- Hoo Fatt, M. S., & Ouyang, X. (2007). Integral-based constitutive equation for rubber at high strain rates. *International Journal of Solids and Structures*, 44, 6491–6506. https://doi.org/10.1016/j.ijsolstr.2007.02.038
- Hossain, M., Navaratne, R., & Perić, D. (2020). 3D printed elastomeric polyurethane: Viscoelastic experimental characterizations and constitutive modelling with nonlinear viscosity functions. *International Journal of Non-Linear Mechanics*, 126, Article 103546. https://doi.org/10.1016/j.ijnonlinmec.2020.103546
- Koprowski-Theiss, N., Johlitz, M., & Diebels, S. (2011). Characterizing the time dependence of filled epdm. Rubber Chemistry and Technology, 84, 147–165. https://doi.org/10.5254/1.3570527
- Kulkami, S., Khan, K. A., Alhammadi, K., Cantwell, W. J., & Umer, R. (2022). A visco-hyperelastic approach to model rate dependent compaction response of a 3D woven fabric. Composites Part A: Applied Science and Manufacturing, 163, Article 107229.
- Kulkarni, S. S., Bayre, N. M., & Khan, K. A. (2025). Modelling visco-hyperelastic response of silicone based elastomers for soft robotics and foldable structure applications. *International Journal of Engineering Science, 211*, Article 104253. https://doi.org/10.1016/j.ijengsci.2025.104253
- Lee, B., Cho, H., Jeong, S., Yoon, J., Jang, D., Lee, D. K., Kim, D., Chung, S., & Hong, Y. (2022). Stretchable hybrid electronics: Combining rigid electronic devices with stretchable interconnects into high-performance on-skin electronics. *Journal of Information Display, 23*, 163–184. https://doi.org/10.1080/15980316.2022.2070291
- Liao, Z., Hossain, M., Yao, X., Mehnert, M., & Steinmann, P. (2020). On thermo-viscoelastic experimental characterization and numerical modelling of VHB polymer. International Journal of Non-Linear Mechanics, 118, Article 103263. https://doi.org/10.1016/j.ijnonlinmec.2019.103263
- Malik, M. H., Kaczynski, J., Zangl, H., & Roshanghias, A. (2023). Flip chip bonding on stretchable printed substrates; the effects of stretchable material and chip encapsulation. Flexible and Printed Electronics, 8, Article 015004. https://doi.org/10.1088/2058-8585/acb2d9
- Melly, S. K., Liu, L., Liu, Y., & Leng, J. (2021). A review on material models for isotropic hyperelasticity. *International Journal of Mechanical System Dynamics*, 1, 71–88. https://doi.org/10.1002/msd2.12013
- Mooney, M. (1940). A theory of large elastic deformation. Journal of Applied Physics, 11, 582-592. https://doi.org/10.1063/1.1712836
- Ogden, R. W. (1972). Large deformation isotropic elasticity On the correlation of theory and experiment for incompressible rubberlike solids. *Proceedings of the Royal Society of London, Series A, Mathematical and Physical Sciences*, 326, 565–584. https://doi.org/10.1098/rspa.1972.0026
- Ogden, R. W., & Roxburgh, D. G. (1999). A pseudo–elastic model for the Mullins effect in filled rubber. Proceedings of the Royal Society of London, Series A, Mathematical and Physical Sciences, 455, 2861–2877.

- Pei, P., Du, Y., Miao, Y., & Suo, T. (2024). Novel hyper-viscoelastic approach to modelling elastomer mechanic behaviour with relaxation spectrum. *Polymer Testing*, 133, Article 108375. https://doi.org/10.1016/j.polymertesting.2024.108375
- Pipkin, A. C., & Rogers, T. G. (1968). A non-linear integral representation for viscoelastic behaviour. *Journal of the Mechanics and Physics of Solids*, 16, 59–72. https://doi.org/10.1016/0022-5096(68)90016-1
- Rajagopal, K. R., & Wineman, A. S. (1992). A constitutive equation for nonlinear solids which undergo deformation induced microstructural changes. *International Journal of Plasticity*, 8, 385–395.
- Rivlin, R. S. (1948). Large elastic deformations of isotropic materials IV. Further developments of the general theory. *Philosophical Transactions of the Royal Society of London, Series A*, 241, 379–397. https://doi.org/10.1098/rsta.1948.0024
- Rivlin, R. S. (1948). Large elastic deformations of isotropic materials. IV. Further developments of the general theory. *Philosophical Transactions of the Royal Society of London. Series A, Mathematical and Physical Sciences*, 241(835), 379–397.
- Simo, J. C. (1998). Computational inelasticity. New York: Springer-Verlag. https://doi.org/10.1007/b98904
- Trung, T. Q., & Lee, N. (2017). Recent progress on stretchable electronic devices with intrinsically stretchable components. Advanced Materials, 29, Article 1603167. https://doi.org/10.1002/adma.201603167
- Valanis, K. C., & Landel, R. F. (1967). The strain-energy function of a hyperelastic material in terms of the extension ratios. *Journal of Applied Physics*, 38, 2997–3002. https://doi.org/10.1063/1.1710039
- Wang, M. C., & Guth, E. (1952). Statistical theory of networks of non-Gaussian flexible chains. *The Journal of Chemical Physics*, 20, 1144–1157. https://doi.org/10.1063/1.1700682
- Wang, S., Nie, Y., Zhu, H., Xu, Y., Cao, S., Zhang, J., Li, Y., Wang, J., Ning, X., & Kong, D. (2022). Intrinsically stretchable electronics with ultrahigh deformability to monitor dynamically moving organs. Science Advances, 8, eabl5511. https://doi.org/10.1126/sciadv.abl5511
- Wineman, A. (2009). Nonlinear viscoelastic solids—a review. Mathematics and Mechanics of Solids, 14, 300-366. https://doi.org/10.1177/1081286509103660
- Wu, W. (2019). Stretchable electronics: Functional materials, fabrication strategies and applications. Science and Technology of Advanced Materials, 20, 187–224. https://doi.org/10.1080/14686996.2018.1549460
- Yang, G., Sun, Y., Qin, L., Li, M., Ou, K., Fang, J., & Fu, Q. (2021). Direct-ink-writing (DIW) 3D printing functional composite materials based on supra-molecular interaction. Composites Science and Technology, 215, Article 109013. https://doi.org/10.1016/j.compscitech.2021.109013
- Yang, L. M., Shim, V. P. W., & Lim, C. T. (2000). A visco-hyperelastic approach to modelling the constitutive behaviour of rubber. *International Journal of Impact Engineering*, 24, 545–560. https://doi.org/10.1016/S0734-743X(99)00044-5
- Yeoh, O. H. (1990). Characterization of elastic properties of carbon-black-filled rubber vulcanizates. Rubber Chemistry and Technology, 63, 792-805.